Received: 6 September 2022 | Revised: 8 February 2023 | Accepted: 28 February 2023

DOI: 10.1002/asna.20220060

Astronomische Nachrichten

ORIGINAL ARTICLE

On the origin of de-polarization in CB54

Niko Zielinski[1] | **Sebastian Wolf**[1] | **Kate Pattle**[2]

[1]Institute of Theoretical Physics and Astrophysics, University of Kiel, Leibnizstrasse 15 Kiel, 24118, Germany

[2]Department of Physics and Astronomy, University College London, Gower Street London, WC1E 6BT, United Kingdom

Correspondence
Niko Zielinski, Institute of Theoretical Physics and Astrophysics, University of Kiel, Leibnizstrasse 15, Kiel, 24118, Germany.
Email: nzielinski@astrophysik.uni-kiel.de

Funding information
DLR/BMBF, Grant/Award Number: 50OR1910.; Royal Society, Grant/Award Number: URF\R1\211322.

Abstract

We present polarimetric observations of the Bok globule CB54 in the far-infrared via SOFIA/HAWC+ bands D (154 μm) and E (214 μm). We detect polarization with mean polarization degrees of $\overline{p_{154\,\mu\mathrm{m}}} = 7.7\,\% \pm 5.4\%$ and $\overline{p_{214\,\mu\mathrm{m}}} = 8.5\,\% \pm 5.4\,\%$ at 154 and 214 μm, respectively. The polarization degree decreases toward the inner region of CB54, revealing a "polarization hole". This finding can be explained by the impact of dichroic absorption counteracting the effect of polarized emission. The same effect allows us to explain the observed wavelength-dependent orientation of the linear polarization in the dense, central region of CB54. The polarization pattern appears uniform at core scales but un-ordered at larger scales—similar to what was found in previous studies of this object. The mean polarization angle amounts to $\overline{\theta_{154\,\mu\mathrm{m}}} = 62.4 \pm 44.5°$ and $\overline{\theta_{214\,\mu\mathrm{m}}} = -80.1 \pm 60.0°$ at 154 and 214 μm, respectively.

KEYWORDS

instrumentation: polarimeters, ISM: magnetic fields, polarization

1 | INTRODUCTION

While huge efforts have been put into studying the process of star formation, major open questions—such as concerning the role of turbulence or the origin of the stellar initial mass function—still remain (McKee & Ostriker 2007; Motte et al. 2018). Another key element is the role that magnetic fields play during the different evolutionary stages between molecular clouds and main-sequence stars (e.g., André et al. 2014; Hull & Zhang 2019; Le Gouellec et al. 2022; Matthews & Wilson 2002; Pudritz et al. 2013; Seifried & Walch 2015). For example, magnetic fields are used to explain the observed low star formation rates per freefall time by slowing down the contraction of star-forming regions and filaments (Federrath 2015; Van Loo et al. 2015). Moreover, magnetic fields are expected to impact the coupling of dust and gas as well as the structure of cloud fragments (e.g., Wolf et al. 2003). An important approach to achieve further progress in these fields is to measure the strength and structure of magnetic fields during the individual stages of the star formation process. In this context, a well-established technique is polarimetric oberservations of the thermal re-emission radiation. In the case of star-forming clouds, it is generally accepted that polarization at submillimeter/millimeter wavelengths is primarily due to thermal re-emission radiation by non-spherical dust grains, which are aligned with respect to the ambient magnetic field, thus providing constraints on the magnetic field. While various concepts describing the potential alignment mechanisms exist, the alignment due to radiative torques (RATs) seems to be the most promising one in this particular environment (for a review refer to, e.g., Andersson et al. 2015). The alignment of dust grains due to RATs results from different extinction

cross sections for left- and right-hand components of the circular polarization of light incident upon a nonspherical dust grain. This asymmetry leads to torques on the dust grain, which result in an increased angular momentum. A net internal magnetization results from the Barnett effect (Barnett 1915), if the dust grains are composed of paramagnetic material. In the presence of an external magnetic field, the magnetized grain Larmor precesses around the field direction (Andersson et al. 2015; Draine & Weingartner 1996; Hoang & Lazarian 2009; Lazarian & Hoang 2007). The alignment of the grain and the magnetic field is thus due to the influence of radiative torques over the precession period, aligning the angular momentum of the grain with the magnetic field (Andersson et al. 2015). If the origin of polarization can be ascribed to the emission from nonspherical dust grains aligned with respect to the magnetic field, it is possible to draw conclusions about the underlying magnetic field strength and structure.

Bok globules are ideal objects to study star formation, since they are often isolated and have rather simple spherical shapes (Bok & Reilly 1947). Polarimetric observations of these objects show an interesting behavior of their polarization pattern: In multiple observations, Bok globules revealed a decrease of the degree of polarization toward their central, more dense regions ("polarization holes", e.g., Henning et al. 2001; Hull et al. 2020; Leach et al. 1991; Minchin & Murray 1994; Wolf et al. 2003; Zielinski et al. 2021). While several mechanisms have been proposed to explain this phenomenon, an all-encompassing unequivocal explanation has not yet been found. Possible mechanisms are an increasing loss of alignment of the dust grains due to higher density and temperature (Goodman et al. 1992) or at high visual extinctions A_V (Whittet et al. 2008), an inability to resolve potentially more complex magnetic field structures on scales below the resolution provided by the instrument beam (e.g., Shu et al. 1987; Wolf et al. 2004), or the destruction of large dust grains into smaller ones ("radiative torque disruption", RATD; Hoang et al. 2019). In addition, a sufficiently high optical depth of these objects at the wavelength of the polarization measurement also provides an explanation of this phenomenon (Brauer et al. 2016). In the latter case, the observed decrease of the degree of polarization toward denser regions is attributed to dichroic absorption. If dichroic (foreground) absorption exceeds the polarized emission the polarization direction flips by 90° (Brauer et al. 2016; Reissl et al. 2014). This is because aligned elongated dust grains absorb more efficiently along their longer axis, causing a net polarization perpendicular to this axis, while thermal emission is polarized along this axis. This effect was detected in the cases of the young stellar object (YSO) NGC1333 IRAS4A (Ko et al. 2020) and the molecular cloud OMC-3 (Liu 2021).

In order to test the hypothesis of the interaction between the two opposing polarization mechanisms, observations at multiple wavelengths are required to constrain the properties of the dust and thus to assess the relative contribution of both counteracting polarization mechanisms.[1] The Bok globule CB54 as an example for a molecular cloud with ongoing star formation (Ciardi & Gómez Martín 2007; de Gregorio-Monsalvo et al. 2009; Gómez et al. 2006) is best suited for this test, since it has been well observed with existing polarimeters at optical and submillimeter/millimeter wavelengths (e.g., Bertrang et al. 2014; Henning et al. 2001; Hull et al. 2014; Matthews et al. 2009; Pattle et al. 2022; Sen et al. 2000; Sen et al. 2005; Sen et al. 2021).

CB54 (also known as LBN 1042, Lynds 1965) is located at a distance of 1.5 kpc (Launhardt & Henning 1997), harbors multiple sources (Ciardi & Gómez Martín 2007; Yun 1996), and is rather massive (∼70–100 $M_\odot$, Launhardt & Henning 1997; Henning et al. 2001). Several molecular outflows have been detected in CB54 (Hull et al. 2014; Yun & Clemens 1994). The goal of this study is to discuss the interplay of polarized emission and dichroic absorption as a possible explanation for the "polarization hole" as well as for the wavelength-dependent orientation of the linear polarization toward the densest region of CB54. We will do so by using observations obtained with the High-resolution Airborne Wideband Camera Plus (HAWC+) onboard SOFIA at two wavelengths—154 μm (band D) and 214 μm (band E). Additionally, we take the polarimetric observations obtained at 850 μm with JCMT/SCUBA into account (Henning et al. 2001; Matthews et al. 2009).

This paper is organized as follows: In Section 2, we describe the data acquisition and reduction. In Section 3, we present the polarization maps and discuss the derived magnetic field structure in Section 3.2. Here, we show a comparison between the magnetic field structures derived at the two SOFIA/HAWC+ wavelengths as well as at 850 μm (archival JCMT/SCUBA observation) and discuss the interaction between dichroic extinction and emission as a possible origin of the observed de-polarization toward the core (see Section 3.2.1). Furthermore, we discuss our results of the magnetic field structure in the context of additional polarimetric observations (see Section 4). We summarize our results in Section 5. Additionally, in the Appendix, we provide a study regarding constraints on dust properties in CB54.

[1] For more detailed information about this process in particular, see appendix B in Reissl et al. (2014).

2 | OBSERVATIONS AND DATA ACQUISITION

The observations of CB54 using the imaging polarimeter HAWC+ onboard SOFIA at band D and E were performed on 28 September 2018 as part of SOFIA Cycle 6 (Proposal 06_0076). Band D and E provide an angular resolution of 13.6″ and 18.2″ full width at half maximum (FWHM) at the 154 μm and 214 μm center wavelengths, respectively. The detector format consists of two 64 × 40 arrays—"R-pol" array and "T-pol" array for detecting reflected and transmitted light, respectively. The "R-pol" array comprises two 32 × 40 sub-arrays, while the "T-pol" array comprises one (Harper et al. 2018). The exposure time for CB54 was 430 and 869 s for band D and E, respectively. The observation mode was a two position chop and nod with a chop frequency of 10.2 Hz. The chop throw was 500″ and the chop angle was 0° for both bands. The nod-time amounted to 40 s and the dither scale was 20″ and 27″ for band D and E, respectively.

The raw data were processed by the HAWC+ instrument team using the data reduction pipeline version 2.0.0. This pipeline consists of different data processing steps including, for instance, corrections for dead pixels, as well as the intrinsic polarization of the instrument and telescope and flux correction based on a standard atmospheric opacity model (for a brief description of all steps, see for instance Santos et al. 2019), resulting in "Level 4" (science-quality) data. These include FITS images of the total intensity (Stokes I), polarization degree p, polarization angle θ, Stokes Q and Stokes U, and related measurement uncertainties. The polarization degree p is given by

$$p = \frac{\sqrt{Q^2 + U^2}}{I} \, . \tag{1}$$

De-biasing of the polarization degree is done using the approach of Wardle & Kronberg (1974) and is part of the HAWC+ reduction pipeline (see e.g., Gordon et al. 2018, for more details). The polarization angle θ is given by

$$\theta = \frac{90}{\pi} \tan^{-1} \left(\frac{U}{Q} \right) . \tag{2}$$

Furthermore, to increase the reliability of our subsequent analysis, we apply three additional criteria for the data that will be considered:

$$\frac{I}{\sigma_I} > 5 \, , \tag{3}$$

$$\frac{p}{\sigma_p} > 2 \, , \tag{4}$$

$$p < 20\%, \tag{5}$$

where σ_I and σ_p are the standard deviations of I and p, respectively. Despite criteria (3) and (4), we find unreasonably high values for the polarization degree. Therefore, we adopt criterion (5), since 20 % is the maximum degree of polarization observed with Planck (Planck Collaboration et al. 2015). We explicitly note that our selected selection criterion with regard to the signal-to-noise ratio of the polarization degree (Equation 4) is below the commonly used value of three for polarization measurements. In total, we obtain 39 and 46 Nyquist-sampled measurements at 154 and 214 μm, respectively, which meet criteria (3), (4), and (5) .

3 | RESULTS

3.1 | Polarization map of CB54

The resulting band D (154 μm, left) and E (214 μm, right) polarization maps of CB54 are shown in Figure 1, overlaid on the respective intensity maps. We find a disordered polarization pattern at both wavelengths. The mean polarization angle is $\overline{\theta}_{\rm D} = 62.4 \pm 44.5°$ and $\overline{\theta}_{\rm E} = -80.1 \pm 60.0°$ for band D and E, respectively. For both wavelengths the degree of polarization varies between 0.5 % and ∼ 20 % and the related errors between 0.2 and ∼ 8 %. The polarization degree is in general higher at 214 μm ($\overline{p_{214\,\mu\rm m}} = 8.5\,\% \pm 5.4\,\%$) than at 154 μm ($\overline{p_{154\,\mu\rm m}} = 7.7\,\% \pm 5.4\,\%$). For both wavelengths, the degree of polarization decreases with increasing intensity, revealing the phenomenon of the so-called "polarization hole", which is often observed in Bok globules and other star-forming regions in the far-infrared to submillimeter–millimeter (submm–mm) wavelength range (e.g., Leach et al. 1991; Minchin & Murray 1994; Henning et al. 2001; Wolf et al. 2003; Vallée et al. 2003; Chuss et al. 2019; Lee et al. 2021; Zielinski et al. 2021, see Section 1 for a brief summary of mechanisms that potentially allow explaining this phenomenon).

3.1.1 | p versus $I/I_{\rm max}$

In the following, we analyze the correlation between the polarization degree p and corresponding intensity I, with the intensity normalized to the maximum intensity $I_{\rm max}$ (see Figure 2). Assuming optically thin emission (an assumption that we will have to drop at later stages of this analysis) and a constant dust temperature, the relationship between polarization degree p and intensity I

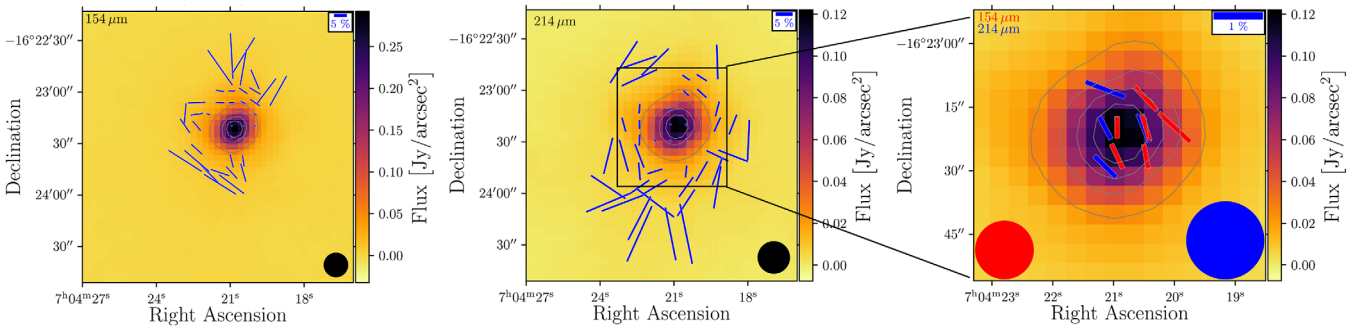

FIGURE 1 *Left/ Middle:* SOFIA/HAWC+ band D (154 μm, left) and E (214 μm, middle) polarization maps of CB54. The total intensity is shown with overlaid electric field polarization vectors in blue. The length of the vectors is proportional to the polarization degree and the direction gives the orientation of the linear polarization. The isocontour lines mark 20, 40, 60, and 80% of the maximum intensity. According to the criteria (3), (4), and (5) only vectors with $I > 5\ \sigma_I$, $p > 2\ \sigma_p$, and $p < 20\%$ are considered (see Section 2). The beam sizes of 13.6″ at 154 μm and 18.2″ at 214 μm (defined by the FWHM) are indicated in the lower right corners of their corresponding plots. *Right:* Zoom-in of the central region of CB54. Here, in addition to criteria (3), (4), and (5), only vectors with $I > 60\ \%I_{\max}$ are shown. Polarization vectors for 154 μm (214 μm) are shown in red (blue).

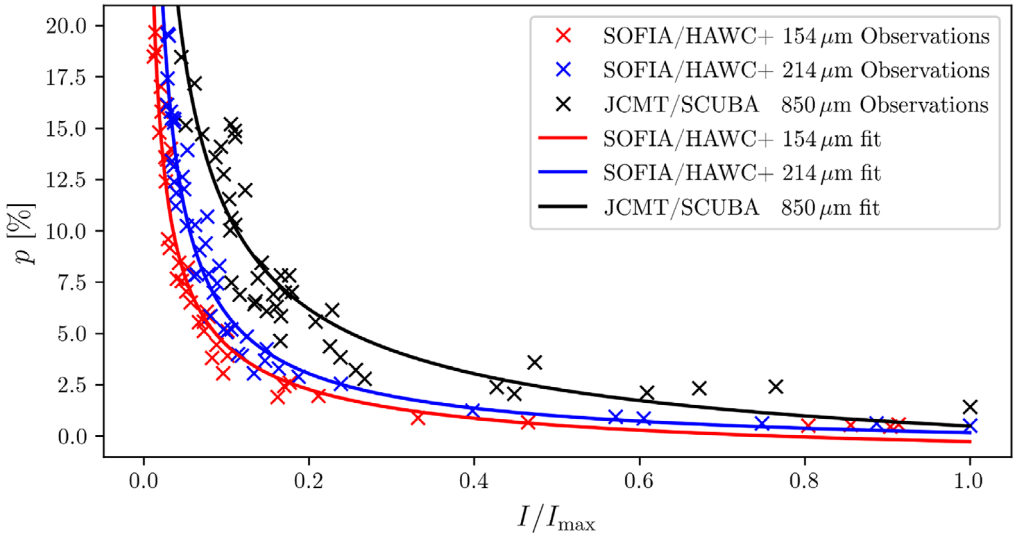

FIGURE 2 Polarization degree at 154 μm (red), 214 μm (blue), and 850 μm (black) as a function of the intensity, scaled to the maximum value. The fitting equation is Equation (6).

is equal to the relation between p and column density. We find that the degree of polarization decreases from $\sim$ 20% to $\lesssim$ 1% with increasing density at both wavelengths, see Figure 2. In addition to the SOFIA/HAWC+ observations, we also consider the polarization measurements at 850 μm obtained with JCMT/SCUBA (Henning et al. 2001, re-reduced by Matthews et al. 2009, angular resolution is 13.8″). We consider the data presented in Matthews et al. (2009) and apply the same selection criteria as for our SOFIA/HAWC+ data (criteria 3, 4, and 5, see Figure 2). Henning et al. (2001) investigated the p vs. I dependency for the two Bok globules CB54 and DC253-1.6. For this purpose, they extended the approach of Davis et al. (2000), who described the relation of p vs. I in the case of the serpens cloud core using linear fits, by adopting a power law. They approximated the decrease in the polarization degree as a function of increasing intensity using the equation

$$p = a_0 + a_1 \cdot \left(\frac{I}{I_{\max}}\right)^{a_2}, \tag{6}$$

where a_0, a_1, and a_2 are fitting parameters. We perform the same analysis as Henning et al. (2001) and obtain for CB54 $a_{0,154\ \mu m} = -1.75 \pm 0.99$, $a_{1,154\ \mu m} = 1.47 \pm 0.48$, $a_{2,154\ \mu m} = -0.62 \pm 0.07$ and $a_{0,214\ \mu m} = -0.97 \pm 0.97$, $a_{1,214\ \mu m} = 1.13 \pm 0.42$, $a_{2,214\ \mu m} = -0.79 \pm 0.10$. The parameter a_2, which describes the slope of $p(I)$, is slightly

TABLE 1 Overview of all calculated a_2 values that describe the slope of the polarization decrease for different objects and wavelengths.

Object	Wavelength (μm)	Instrument	a_2	Reference
CB54	154	SOFIA/HAWC+	-0.62 ± 0.07	This article
CB54	214	SOFIA/HAWC+	-0.79 ± 0.10	This article
CB54	850	JCMT/SCUBA	-0.64 ± 0.01	Henning et al. (2001)
CB54	850	JCMT/SCUPOL	-0.61 ± 0.16	This article
OMC-3	154	SOFIA/HAWC+	-0.51 ± 0.04	Zielinski & Wolf (2022)
OMC-3	214	SOFIA/HAWC+	-0.63 ± 0.05	Zielinski & Wolf (2022)
B335	214	SOFIA/HAWC+	-0.55 ± 0.22	Zielinski et al. (2021)
B335	850	JCMT/SCUBA	-0.43	Wolf et al. (2003)
DC 253-1.6	850	JCMT/SCUBA	-0.55 ± 0.02	Henning et al. (2001)

higher at 214 μm. Interestingly, comparing this slope to those reported in the previous studies for Bok globules and molecular clouds, one can see that the slopes are similar. Henning et al. (2001) did the same analysis for CB54 at 850 μm and obtained $a_{2,850\ \mu\mathrm{m}} = -0.64$. Using the re-reduced SCUBA data for CB54 (Matthews et al. 2009), we get $a_{2,850\ \mu\mathrm{m}} = -0.61$. Wolf et al. (2003) derived $a_{2,850\ \mu\mathrm{m}} = -0.43$ for the Bok globule B335 using JCMT/SCUBA, while Zielinski et al. (2021) obtained $a_{2,214\ \mu\mathrm{m}} = -0.55$ with SOFIA/HAWC+. In Table 1 we provide an overview of all values of the parameter a_2 derived for different objects and wavelengths. As the fitting parameter a_2 provides a quantitative measure of the "polarization hole", similar values might indicate the occurrence of the same underlying mechanism(s). However, a thorough analysis of this hypothesis—and corresponding spread of possible values of that parameter that allows us to verify this hypothesis—would require dedicated numerical simulations, which are beyond the scope of the current study.

The degree of polarization decreases with increasing intensity for all three wavelengths. In addition, it can be seen that—at the same distance from the core of CB54—the degree of polarization increases with wavelength. This raises the question which dust properties (axis ratio and dust grain size) are consistent with this finding. An approach to derive constraints on the dust properties of CB54 is presented in the Appendix.

3.1.2 | p versus I

In addition to Section 3.1.1, the relation between p and (not-normalized) intensity has been often adopted to study grain alignment (e.g. Coudé et al. 2019; Jones et al. 2015; Kwon et al. 2022) by fitting $p \propto I^{\alpha}$ to the measured polarization data, see Figure 3. A slope of $\alpha = -1$ implies no grain alignment beyond a certain A_V. We obtain $\alpha_{154\ \mu\mathrm{m}} = -0.74 \pm 0.05$, $\alpha_{214\ \mu\mathrm{m}} = -0.88 \pm 0.03$ and $\alpha_{850\ \mu\mathrm{m}} = -0.80 \pm 0.03$, indicating that the polarization is not limited to the periphery of the Bok globule. These results are similar to those reported in earlier studies, e.g., Coudé et al. (2019) found $\alpha = -0.85 \pm 0.01$ for the Perseus B1 star-forming region, Soam et al. (2018) found $\alpha \approx -0.9$ for Ophiuchus-B, Matthews & Wilson (2002) found $\alpha \approx -0.8$ for B1 using SCUPOL measurements and Pattle et al. (2019) found $\alpha \approx -0.6$ to -0.7 for Ophiuchus B and C.

3.2 | Magnetic field structure of CB54

Assuming that the observed polarization is due to the emission from nonspherical dust grains aligned with respect to the magnetic field, we can obtain the projection of the magnetic field direction on the plane of the sky integrated along the line-of-sight (from here on: magnetic field direction) by rotating the polarization vectors by 90°. The magnetic field direction appears disordered at large scales at both wavelengths, but mostly uniform at the center of CB54 (see Figure 4). This finding is similar to existing polarimetric observations of CB54 at similar scales (Henning et al. 2001; Matthews et al. 2009).

3.2.1 | Comparing the magnetic field structure at 154 μm, 214 μm and 850 μm

In the following, we compare the results obtained by SOFIA/HAWC+ at 154 and 214 μm and SCUBA at 850 μm. In order to obtain a comprehensive comparison between

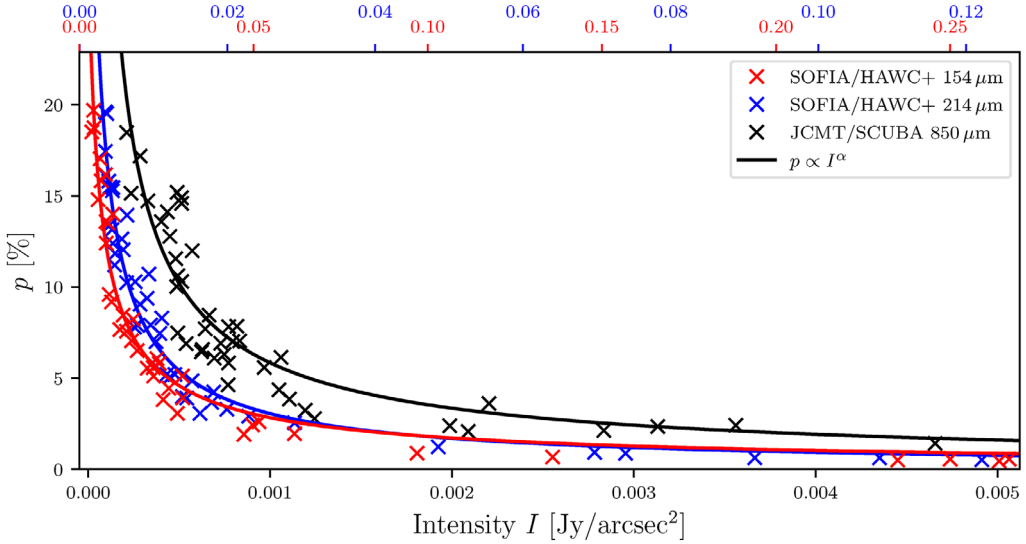

FIGURE 3 Polarization degree at 154 μm (red), 214 μm (blue), and 850 μm (black) as a function of the intensity.

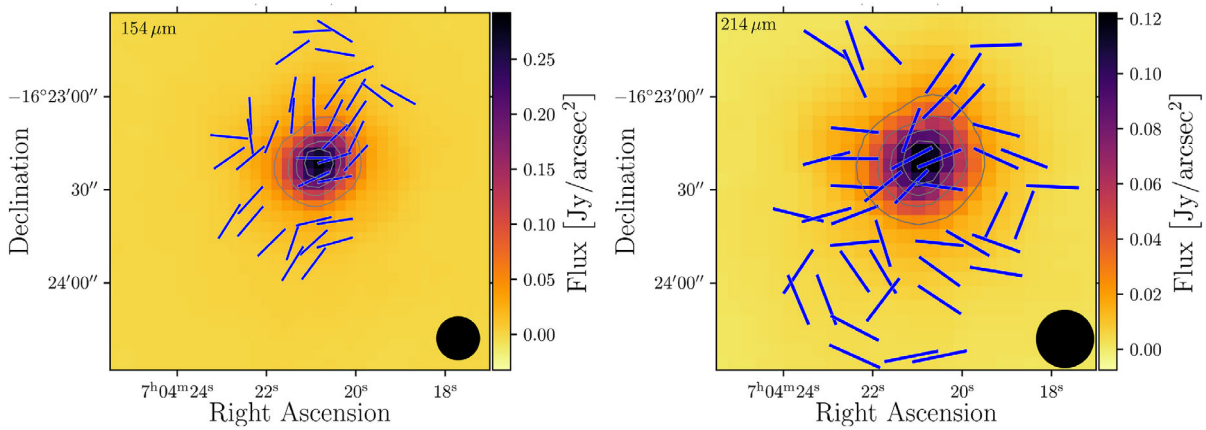

FIGURE 4 SOFIA/HAWC+ intensity maps of CB54 at 154 μm (left) and 214 μm (right). Assuming that the detected polarization is caused by magnetically aligned nonspherical dust grains, the magnetic field direction is displayed by rotating the polarization vectors by 90°. The isocontour lines mark 20, 40, 60, and 80% of the maximum intensity. According to criteria (3) to (5) only vectors with $I > 5\ \sigma_I$, $p > 2\ \sigma_p$, and $p < 20\%$ are considered (see Section 2). The beam sizes of 13.6″ at 154 μm and 18.2″ at 214 μm (defined by the FWHM) are indicated in the lower right.

the different polarization observations of CB54, all maps are compiled in Figure 5.

We perform a pairwise comparison of the derived magnetic field directions, i.e., at wavelengths of 154 μm/214 μm, 214 μm/850 μm, and 154 μm/850 μm. As the pixel scale of the observational data is wavelength-dependent, we sample all data on a grid with pixel size 9.1″x 9.1″, i.e., twice the pixel size of band E. Subsequently, we calculate the smallest deviation ($\Delta\theta$) between the local magnetic field direction, i.e., of each individual pixel, provided that measurements of the underlying polarization degrees at both wavelengths fulfill our selection criteria (3) to (5). In addition, we calculate the smallest signed deviation ($\delta\theta$) to see if the differences in local magnetic field directions are ordered, i.e., if deviations are primarily clockwise (+) or counter-clockwise (−).

For the calculation of the deviations $\Delta\theta$ and $\delta\theta$ the measurement uncertainties, i.e., the 1σ interval for a given magnetic field direction is taken into account (see Figure 6 and Table 2).

The least deviation can be found between 214 μm and 850 μm across CB54 and for the central regions (i.e., $I > 0.4\, I_{\max}$) between 154 and 214 μm. The highest deviation can be found between 154 and 850 μm across CB54. While the polarization angles in the central region are consistent for 154 μm↔214 μm, they deviate in the central regions for 214 μm↔850 μm and 154 μm↔850 μm, especially in

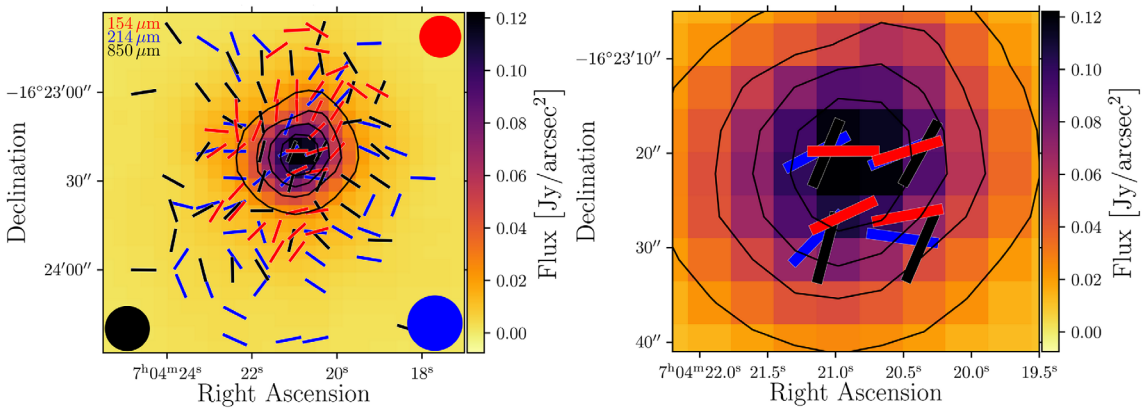

FIGURE 5 *Left:* SOFIA/HAWC+ intensity map of CB54 at 214 μm. The isocontour lines mark 20, 40, 60, and 80% of the maximum intensity. The total intensity is shown with overlaid polarization vectors in red (154 μm), blue (214 μm) and black (850 μm). The vectors have been set to a fixed length and are rotated by 90° to trace the magnetic field direction. The beam sizes of 13.6″ at 154 μm, 18.2″ at 214 μm and 14.7″ at 850 μm (defined by the FWHM) are indicated in the upper right, lower right and lower left, respectively. *Right:* Zoom-in on the central region of CB54.

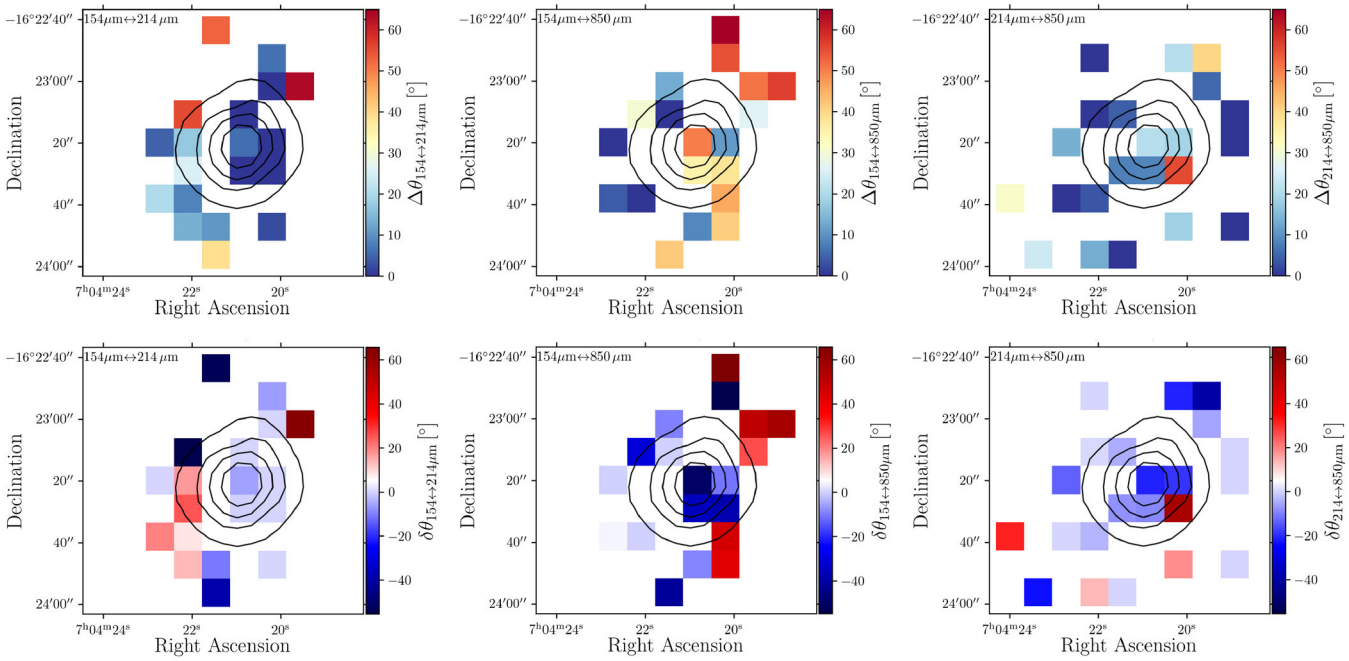

FIGURE 6 Comparison between the magnetic field directions derived using SOFIA/HAWC+ and SCUPOL observations. Color scale shows the smallest deviation $\Delta\theta$ (*top layer*) and the smallest signed deviation $\delta\theta$ (*bottom layer*) between polarization vectors at the respective wavelengths within one pixel. The isocontour lines mark 20%, 40%, 60%, and 80% of the maximum intensity. *Left:* Comparison between 154 and 214 μm. *Middle:* Comparison between 154 and 850 μm. *Right:* Comparison between 214 and 850 μm. See Section 3.2.1 for the corresponding analysis.

TABLE 2 Overview of the comparison (mean (un-)signed deviations) between the different magnetic field orientations. The smallest un-signed deviation is denoted with $\Delta\theta$ and the smallest signed deviation with $\delta\theta$. The central region marks the region where $I > 0.4 \cdot I_{\max}$, see isocontour lines in Figure 6.

λ_1 (μm)	λ_2 (μm)	$\overline{\Delta\theta}$	$\overline{\Delta\theta}$ (central region)	$\overline{\delta\theta}$	$\overline{\delta\theta}$ (central region)
154	214	17.1 ± 11.8°	1.2 ± 11.6°	−1.2 ± 11.8°	−1.2 ± 11.6°
154	850	30.2 ± 10.7°	26.8 ± 9.1°	0.69 ± 10.7°	−26.8 ± 9.1°
214	850	13.7 ± 11.3°	19.4 ± 10.9°	−2.36 ± 11.3°	−0.93 ± 10.9°

the latter case. Interestingly, the smallest signed deviation in the innermost center increases with increasing ratio between the two wavelengths of interest, i.e. $\delta\theta = -6°$ for 154 μm↔214 μm, $\delta\theta = -21°$ for 214 μm↔850 μm and $\delta\theta = -50°$ for 154 μm↔850 μm. A likely explanation for this behavior is an increasing optical depth with decreasing wavelength. Only taking the core region into account, see Figure 5 (right), one finds that the magnetic field vectors at 154 μm and 850 μm deviate by $\sim 70°$ ($\pm 20°$).

A "flip" of as much as $\sim 90°$ was proposed by Brauer et al. (2016) and can be explained as follows: As long as the globule is optically thin at a given wavelength, the net polarization of the polarized thermal re-emission radiation of aligned nonspherical dust grains increases with increasing column density. However, once absorption becomes significant, for example, at the central dense regions of CB54 (and at shorter wavelengths), the polarization degree decreases toward the globule core due to dichroic extinction. This effect can even induce a reversal of the polarization direction by 90° if the dichroic extinction predominates—for a sufficiently high optical depth—over the dichroic emission. We note that dichroic extinction is likely to be important at shorter wavelengths. At the same time, the counter-acting effects of polarized emission and dichroic extinction provide a possible explanation for the decrease of the degree of polarization with increasing intensity, see Figure 2, since the optical depth is increasing with intensity. This is one of the first times that the proposed effect could be observed in Bok globules.[2]

We explicitly point out that this finding is based on data with a lower signal-to-noise ratio than typically considered in the analysis of comparable polarization observations. Therefore, this result should be taken as an indication that the impact of the described optical depth effect might provide a possible explanation of the observed (a) decrease of the polarization degree and (b) wavelength-dependent orientation of the linear polarization. However, we emphasize that this explanation can only be applied for the central region of CB54 (where $I > 0.4 \cdot I_{\max}$). For the case of the Bok globule B335, Zielinski et al. (2021) show that by using the radiative torque mechanism, the combined impact of the interstellar radiation field and the embedded central source allow explaining the decrease of the polarization degree in the outer regions of that source. However, since CB54 contains multiple stellar sources, (Ciardi & Gómez Martín 2007; Yun 1996) shows significantly higher complexity with regard to the magnetic field structure, and the achieved spatial resolution is lower than in the case of B335, a corresponding detailed analysis based on the existing observations is not feasible.

[2]Other examples—from other classes of dust-enshrouded astrophysical objects—are the Class 0 source IRAM 04191 (Soam et al. 2015), the YSO NGC1333 IRAS4A (Ko et al. 2020) and the molecular cloud OMC-3 (Liu 2021).

4 | MAGNETIC FIELD OF CB54 DERIVED FROM POLARIMETRIC OBSERVATIONS AT DIFFERENT WAVELENGTHS AND SPATIAL SCALES

As explained in Section 1, CB54 is a well-studied star-forming Bok globule with existing polarimetric observations covering the optical to submillimeter/millimeter wavelength range (see Figure 7 for an overview). Here, we provide a short summary of selected observations in the context of our observations presented in Section 3.1. We note that in contrast to our observations, the origin of polarization in the optical and near-infrared is solely the absorption of photons of magnetically aligned nonspherical dust grains. In this case, the orientation of the polarization vectors represents the magnetic field direction.

Optical: 0.66 μm (*R* Band):
Sen et al. (2021) observed CB54 using the IUCAA Girawali Observatory in the optical wavelength regime. The detected polarization measurements show a disordered pattern, similar to our results in the far-infrared. The degree of polarization is lower in the optical ($\sim 0.5 < p < 8\,\%$) than in the far-infrared ($0.5 < p < 20\,\%$).

Near-infrared: 1.24 μm (*Js* Band):
Bertrang et al. (2014) observed CB54 using the SOFI/NTT in the near-infrared. While the large-scale magnetic field appears un-ordered as well, the near-infared observations reveal ordered polarization vectors at small scales, similarly to our results. The degree of polarization is lower in the near-infrared ($1 < p < 10\,\%$) than in the far-infared ($0.5 < p < 20\,\%$).

Submm: 850 μm:
Henning et al. (2001) observed CB54 with JCMT/SCUBA on scales similar to SOFIA/HAWC+. We show the re-reduction of these data by Matthews et al. (2009). We compare the polarization angles in Section 3.2.1. The degree of polarization is generally higher at 850 μm than at 154 and 214 μm (see Figure 2).

mm: 1.3 mm:
Hull et al. (2014) observed CB54 as part of the TADPOL survey using CARMA. While the polarization vectors

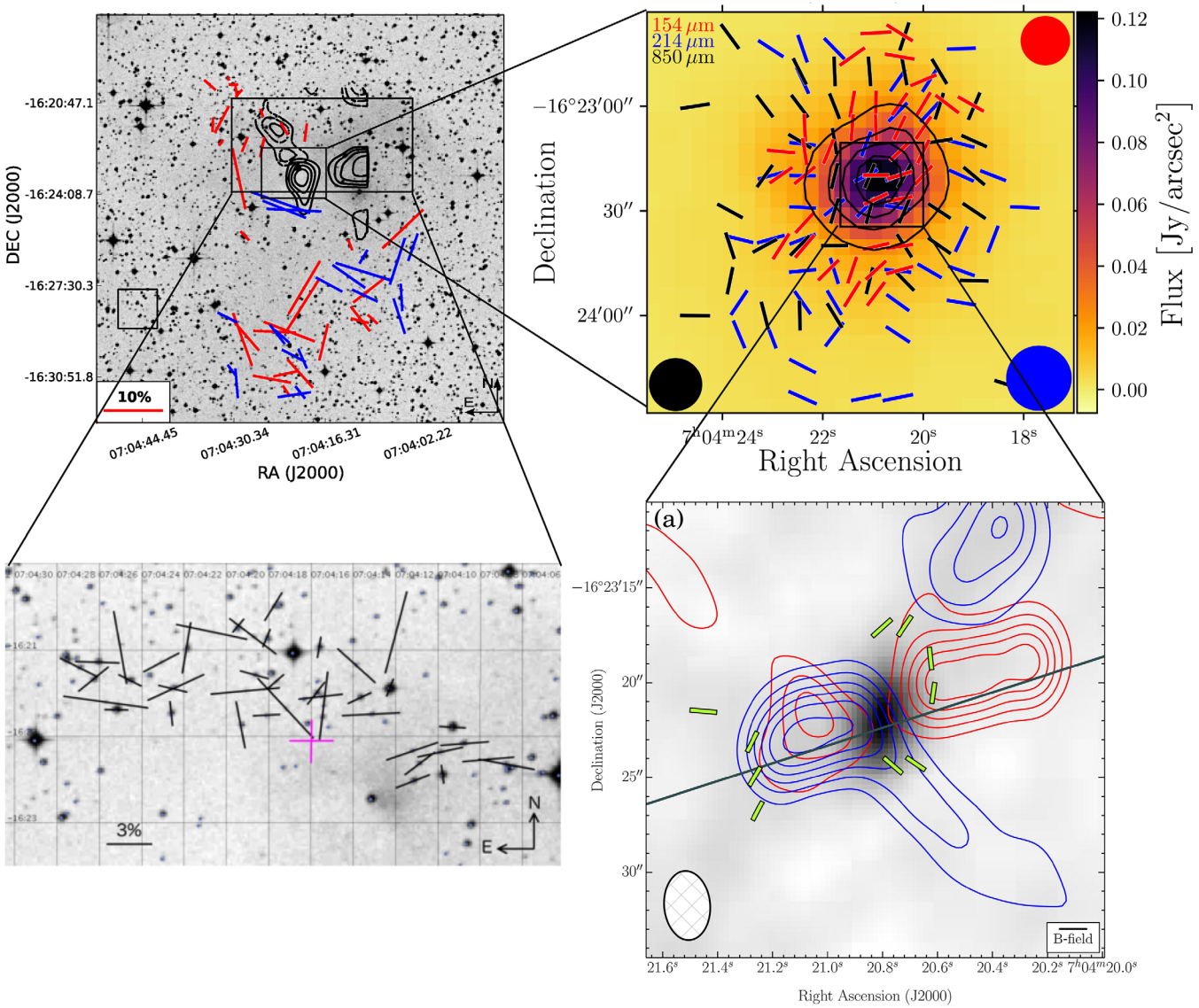

FIGURE 7 Multiwavelength, multiscale polarization maps of CB54. *Top left:* Polarization map of CB54 in the near-IR (*Js* band, 1.24 μm, overlaid on a DSS intensity map; Bertrang et al. 2014) obtained using SOFI/NTT. [Credit: Bertrang et al., A&A, 565, A94, 2014, reproduced with permission ĭ ESO.] The solid contour lines represent the blueshifted (southwestern), and the dotted contour lines represent the redshifted (northeastern) outflow lobe (Yun & Clemens 1994). *Top right:* Magnetic field map of CB54 at 154 μm (red), 214 μm (blue) and 850 μm (black) obtained with SOFIA/HAWC+ and SCUPOL (Henning et al. 2001; Matthews et al. 2009). *Bottom left:* Polarization map of CB54 in the optical (*R* band, 0.66 μm; reuse of figure 1 in Sen et al. 2021) obtained using the IUCAA Girawali Observatory. *Bottom right:* Magnetic field map of CB54 at 1.3 mm, obtained using CARMA (Hull et al. 2014, © AAS. Reproduced with permission).

obtained using HAWC+ show an organized pattern in the central region of CB54, the CARMA results show a more complex pattern. The measured values for the degree of polarization were not specified by Hull et al. (2014).

The magnetic field of CB54 appears un-ordered at these different scales and wavelengths. However, at small scales, i.e., near the core of CB54, the magnetic field shows a more homogeneous pattern. The reason for the detected random large-scale pattern is likely due to the impact of the existing large-scale outflows (Yun & Clemens 1994).

5 | CONCLUSIONS

We studied the magnetic field of CB54 using polarimetric observations obtained with SOFIA/HAWC+ at 154

and 214 μm and archival polarimetric observations with JCMT/SCUBA at 850 μm (Henning et al. 2001; Matthews et al. 2009).

1. The large-scale polarization patterns of CB54 shows a disordered structure at 154 and 214 μm and is rather uniform near the core. The mean polarization angles amount to $\overline{\theta_{154\,\mu\mathrm{m}}} = 62.4 \pm 44.5°$ and $\overline{\theta_{214\,\mu\mathrm{m}}} = -80.1 \pm 60.0°$.
2. Corresponding to the underlying polarization maps, the large-scale magnetic field structure appears disordered toward the outer regions at both wavelengths—similar to previous polarimetric observations of CB54—but rather uniform near the core.
3. The mean polarization degree is $\overline{p_{154\ \mu\mathrm{m}}} = 7.7 \pm 5.8$ % and $\overline{p_{214\ \mu\mathrm{m}}} = 8.5 \pm 5.4$ %. At both wavelengths, the degree of polarization decreases with increasing intensity. The calculated slope for this decrease is similar to existing literature values. We can, for one of the first times in the case of Bok globules, show that the interplay of polarized emission and dichroic absorption provides an explanation for the decrease of the polarization degree as well as for the wavelength-dependent orientation of the linear polarization at the core of CB54.

ACKNOWLEDGMENTS

We thank Stefan Heese for his contribution to successfully applying observing time to obtain the presented SOFIA/HAWC+ measurements. This paper is based on observations made with the NASA/DLR Stratospheric Observatory for Infrared Astronomy (SOFIA). SOFIA is jointly operated by the Universities Space Research Association, Inc. (USRA), under NASA contract NNA17BF53C, and the Deutsches SOFIA Institut (DSI) under DLR contract 50 OK 0901 to the University of Stuttgart. Acknowledgement: N.Z. and S.W. acknowledge the support by the DLR/BMBF grant 50OR1910. K.P. is a Royal Society University Research Fellow, supported by grant number URF\R1\211322. Open Access funding enabled and organized by Projekt DEAL.

CONFLICT OF INTEREST STATEMENT

The authors declare no potential conflict of interests.

DATA AVAILABILITY STATEMENT

The data obtained with SOFIA/HAWC+ and used in this analysis are available in the SOFIA science archive at the Infrared Processing & Analysis Center (IPAC) under AOR ID 06_0076_1 and 06_0076_2.

ORCID

Niko Zielinski https://orcid.org/0000-0002-3542-2583
Sebastian Wolf https://orcid.org/0000-0001-7841-3452
Kate Pattle https://orcid.org/0000-0002-8557-3582

REFERENCES

Acharyya, K., Hassel, G. E., & Herbst, E. 2011, *ApJ*, *732*(2), 73.
Andersson, B. G., Lazarian, A., & Vaillancourt, J. E. 2015, *ARA&A*, *53*, 501.
Andersson, B. G., Lopez-Rodriguez, E., Medan, I., et al. 2022, *ApJ*, *931*(2), 80.
André, P., Di Francesco, J., Ward-Thompson, D., Inutsuka, S. I., Pudritz, R. E., & Pineda, J. E. 2014, in: *Protostars and Planets VI*, eds. H. Beuther, R. S. Klessen, C. P. Dullemond, & T. Henning, University of Arizona Press (Tucson), 27.
Barnett, S. J. 1915, *Phys. Rev.*, *6*(4), 239.
Bertrang, G., Wolf, S., & Das, H. S. 2014, *A&A*, *565*, A94.
Bok, B. J., & Reilly, E. F. 1947, *ApJ*, *105*, 255.
Brauer, R., Wolf, S., & Reissl, S. 2016, *A&A*, *588*, A129.
Chiar, J. E., Adamson, A. J., Whittet, D. C. B., et al. 2006, *ApJ*, *651*(1), 268.
Chuss, D. T., Andersson, B. G., Bally, J., et al. 2019, *ApJ*, *872*(2), 187.
Ciardi, D. R., & Gómez Martín, C. 2007, *ApJ*, *664*(1), 377.
Coudé, S., Bastien, P., Houde, M., et al. 2019, *ApJ*, *877*(2), 88.
Davis, C. J., Chrysostomou, A., Matthews, H. E., Jenness, T., & Ray, T. P. 2000, *ApJ*, *530*(2), L115.
de Gregorio-Monsalvo, I., Gómez, J. F., Anglada, G., Torrelles, J. M., Kuiper, T. B. H., Suárez, O., & Patel, N. A. 2009, *AJ*, *137*(6), 5080.
Draine, B. T. 2003, *ApJ*, *598*(2), 1026.
Draine, B. T., & Lee, H. M. 1984, *ApJ*, *285*, 89.
Draine, B. T., & Malhotra, S. 1993, *ApJ*, *414*, 632.
Draine, B. T., & Weingartner, J. C. 1996, *ApJ*, *470*, 551.
Federrath, C. 2015, *MNRAS*, *450*(4), 4035.
Gómez, J. F., de Gregorio-Monsalvo, I., Suárez, O., & Kuiper, T. B. H. 2006, *AJ*, *132*(3), 1322.
Goodman, A. A., Jones, T. J., Lada, E. A., & Myers, P. C. 1992, *ApJ*, *399*, 108.
Gordon, M. S., Lopez-Rodriguez, E., Andersson, B. G., Clarke, M., Coude, S., Moullet, A., Richards, S. N., Shuping, R. Y., Vacca, W., & Yorke, H. 2018. arXiv e-prints, arXiv:1811.03100.
Harper, D. A., Runyan, M. C., Dowell, C. D., et al. 2018, *J. Astron.l Instrum.*, *7*(4), 1840008–1025.
Henning, T., Wolf, S., Launhardt, R., & Waters, R. 2001, *ApJ*, *561*(2), 871.
Hildebrand, R. H., Dotson, J. L., Dowell, C. D., Schleuning, D. A., & Vaillancourt, J. E. 1999, *ApJ*, *516*(2), 834.
Hoang, T., & Lazarian, A. 2009, *ApJ*, *695*(2), 1457.
Hoang, T., Lazarian, A., & Andersson, B. G. 2015, *MNRAS*, *448*(2), 1178.
Hoang, T., Tram, L. N., Lee, H., & Ahn, S.-H. 2019, *Nat. Astron.*, *3*, 766.
Hull, C. L. H., Le Gouellec, V. J. M., Girart, J. M., Tobin, J. J., & Bourke, T. L. 2020, *ApJ*, *892*(2), 152.
Hull, C. L. H., Plambeck, R. L., Kwon, W., et al. 2014, *ApJS*, *213*(1), 13.
Hull, C. L. H., & Zhang, Q. 2019, *Front. Astron. Space Sci.*, *6*, 3.
Jones, T. J., Bagley, M., Krejny, M., Andersson, B. G., & Bastien, P. 2015, *AJ*, *149*(1), 31.

Kirchschlager, F., Mattsson, L., & Gent, F. A. 2022, *MNRAS*, *509*(3), 3218.
Ko, C.-L., Liu, H. B., Lai, S.-P., Ching, T.-C., Rao, R., & Girart, J. M. 2020, *ApJ*, *889*(2), 172.
Kobus, J., Wolf, S., Ratzka, T., & Brunngräber, R. 2020, *A&A*, *642*, A104.
Kwon, W., Pattle, K., Sadavoy, S., et al. 2022, *ApJ*, *926*(2), 163.
Launhardt, R., & Henning, T. 1997, *A&A*, *326*, 329.
Lazarian, A. 2020. arXiv e-prints, arXiv:2009.11304.
Lazarian, A., & Hoang, T. 2007, *MNRAS*, *378*(3), 910.
Le Gouellec, V. J. M., Maury, A. J., & Hull, C. L. H. 2022. arXiv e-prints, arXiv:2212.11899.
Leach, R. W., Clemens, D. P., Kane, B. D., & Barvainis, R. 1991, *ApJ*, *370*, 257.
Lee, D., Berthoud, M., Chen, C.-Y., et al. 2021, *ApJ*, *918*(1), 39.
Liu, H. B. 2021, *ApJ*, *914*(1), 25.
Lynds, B. T. 1965, *ApJS*, *12*, 163.
Mathis, J. S., Rumpl, W., & Nordsieck, K. H. 1977, *ApJ*, *217*, 425.
Matthews, B. C., McPhee, C. A., Fissel, L. M., & Curran, R. L. 2009, *ApJS*, *182*(1), 143.
Matthews, B. C., & Wilson, C. D. 2002, *ApJ*, *574*(2), 822.
McKee, C. F., & Ostriker, E. C. 2007, *ARA&A*, *45*(1), 565.
Minchin, N. R., & Murray, A. G. 1994, *A&A*, *286*, 579.
Motte, F., Bontemps, S., & Louvet, F. 2018, *ARA&A*, *56*, 41.
Pattle, K., Lai, S.-P., Hasegawa, T., et al. 2019, *ApJ*, *880*(1), 27.
Pattle, K., Lai, S.-P., Sadavoy, S., et al. 2022, *MNRAS*, *515*(1), 1026.
Planck Collaboration,Ade, P. A. R., Aghanim, N., et al. 2015, *A&A*, *576*, A104.
Pudritz, R. E., Klassen, M., Kirk, H., Seifried, D., & Banerjee, R. 2013, *Proc. Int. Astron. Union*, *9*(S302), 10.
Reissl, S., Wolf, S., & Seifried, D. 2014, *A&A*, *566*, A65.
Rilinger, A. M., & Espaillat, C. C. 2021, *ApJ*, *921*(2), 182.
Santos, F. P., Chuss, D. T., Dowell, C. D., et al. 2019, *ApJ*, *882*(2), 113.
Seifried, D., & Walch, S. 2015, *MNRAS*, *452*(3), 2410.
Sen, A. K., Gupta, R., Ramaprakash, A. N., & Tandon, S. N. 2000, *A&AS*, *141*, 175.
Sen, A. K., Il'in, V. B., Prokopjeva, M. S., & Gupta, R. 2021, *MNRAS*, *503*(4), 5274.
Sen, A. K., Mukai, T., Gupta, R., & Das, H. S. 2005, *MNRAS*, *361*(1), 177.
Shu, F. H., Adams, F. C., & Lizano, S. 1987, *ARA&A*, *25*, 23.
Soam, A., Maheswar, G., Lee, C. W., Dib, S., Bhatt, H. C., Tamura, M., & Kim, G. 2015, *A&A*, *573*, A34.
Soam, A., Pattle, K., Ward-Thompson, D., et al. 2018, *ApJ*, *861*(1), 65.
Vaillancourt, J. E., Andersson, B. G., Clemens, D. P., Piirola, V., Hoang, T., Becklin, E. E., & Caputo, M. 2020, *ApJ*, *905*(2), 157.
Vallée, J. P., Greaves, J. S., & Fiege, J. D. 2003, *ApJ*, *588*(2), 910.
Van Loo, S., Tan, J. C., & Falle, S. A. E. G. 2015, *ApJ*, *800*(1), L11.
Voshchinnikov, N. V., & Farafonov, V. G. 1993, *Ap&SS*, *204*(1), 19.
Wardle, J. F. C., & Kronberg, P. P. 1974, *ApJ*, *194*, 249.
Whittet, D. C. B., Hough, J. H., Lazarian, A., & Hoang, T. 2008, *ApJ*, *674*(1), 304.
Wolf, S., Launhardt, R., & Henning, T. 2003, *ApJ*, *592*(1), 233.
Wolf, S., Launhardt, R., & Henning, T. 2004, *Ap&SS*, *292*(1), 239.
Yun, J. L. 1996, *AJ*, *111*, 930.
Yun, J. L., & Clemens, D. P. 1994, *ApJS*, *92*, 145.
Zielinski, N., & Wolf, S. 2022, *A&A*, *659*, A22.
Zielinski, N., Wolf, S., & Brunngräber, R. 2021, *A&A*, *645*, A125.

How to cite this article: Zielinski, N., Wolf, S., & Pattle, K. 2023, *Astron.Nachr./AN*, e20220060. https://doi.org/10.1002/asna.20220060

APPENDIX. CONSTRAINING PROPERTIES OF THE DUST IN CB54 BASED ON THE MEASURED POLARIZATION

The Bok globule CB54 has been observed polarimetrically and on similar scales with HAWC+ and SCUBA. All observations show a decrease of the polarization degree with increasing intensity. If we compare the degree of polarization at the same distance from the core of CB54, see Figure 2, we find an increase of the polarization degree with wavelength. Taking only the region within 0.07 and 0.27 $I/I_{\max}$ into account (see Figure 2), the average polarization degree amounts to $\overline{p_{154\mu m}} = 4.0 \pm 1.4\,\%$, $\overline{p_{214\mu m}} = 5.5 \pm 2.3\,\%$, and $\overline{p_{850\mu m}} = 8.6 \pm 3.6\,\%$ (see Figure A1). This finding triggers the question about the dust properties that are consistent with the observed wavelength-dependence. Moreover, at this distance from the core we can assume that the dust distribution is optically thin at all three wavelengths. Under this assumption, the degree of polarization due to the emission of a nonspherical dust grain can be calculated via

$$p = \frac{C_{\mathrm{abs,l}} - C_{\mathrm{abs,s}}}{C_{\mathrm{abs,l}} + C_{\mathrm{abs,s}}}\,, \tag{A1}$$

where $C_{\mathrm{abs,l}}$ and $C_{\mathrm{abs,s}}$ are the cross sections for absorption in the case of the long and short axis of the dust grain, respectively.

In the following, we conduct a parameter study to constrain selected dust parameters in CB54. We consider two dust phases: pure astrosilicate and a mixture of astrosilicate and graphite, consisting of compact, nonspherical dust grains with optical properties from Draine (2003). The silicate-graphite mixture (hereafter Sil-Graph) has a mass abundance ratio of 62.5% silicate and 37.5% graphite.[3] Whether graphite dust grains align with the magnetic field remains an open question (e.g., Andersson et al. 2022; Chiar et al. 2006; Hildebrand et al. 1999; Hoang et al. 2015; Lazarian 2020). For our parameter study, we assume that the graphite grains are not aligned by the magnetic field.

[3]Graphite has an anisotropic optical behavior. According to its structure, the 1/3 to 2/3 approximation (Draine & Lee 1984; Draine & Malhotra 1993) needs to be applied.

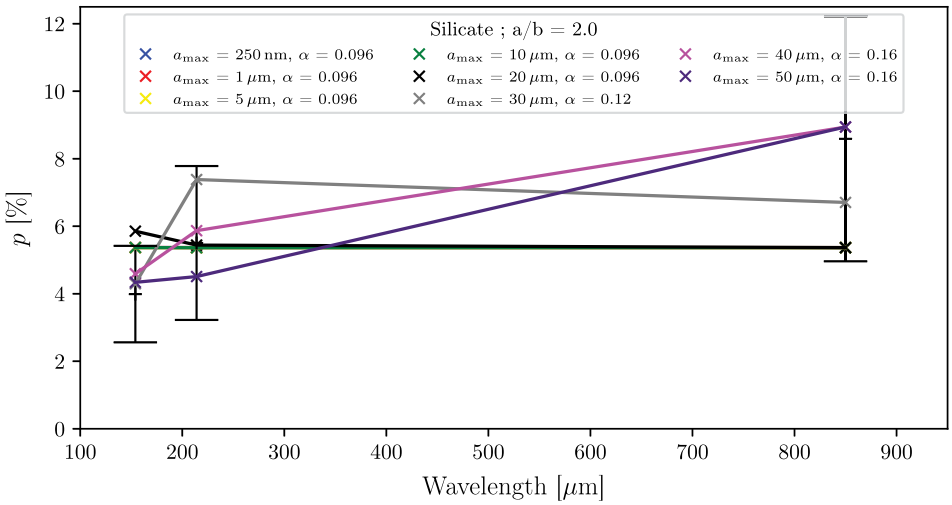

FIGURE A1 Calculated degree of polarization ("x" markers) using Equation (A1) for silicate grains with an axis ratio of 2. Error bars indicate the average polarization degree for the observations at 154, 214, and 850 μm.

TABLE A1 Overview of the parameters considered in the parameter study. Tagged with the symbol "↕" are free parameters.

Parameter	Symbol	Value
Dust composition	(↕)	Silicate, Sil-Graph
Grain size shape		Oblate
Axis ratio	a/b (↕)	1.1 – 4
Grain size distribution exponent		−3.5
Minimum grain radius	a_{min}	5 nm
Maximum grain radius	a_{max} (↕)	50 nm – 50 μm

Furthermore, we assume that the dust grain size distribution is the same as that in the ISM:

$$\mathrm{d}n(a) \propto a^{-3.5}\,\mathrm{d}a, \qquad a_{min} < a < a_{max}, \qquad \text{(A2)}$$

where $\mathrm{d}n(a)$ denotes the number of dust grains with a radius that is in the range $[a, a + \mathrm{d}a]$ (Mathis et al. 1977). While we assume a minimum dust grain size of $a_{min} = 5$ nm, as it is often applied to describe the dust phase of the ISM (e.g., Acharyya et al. 2011; Kirchschlager et al. 2022; Kobus et al. 2020; Rilinger & Espaillat 2021), it is unclear if the same argument is suitable for the maximum grain size ($a_{max} = 250$ nm for the ISM; see e.g., Mathis et al. 1977). For our parameter study we consider maximum dust grain radii between $a_{max} \in (50\,\mathrm{nm} - 50\,\mu\mathrm{m})$. We assume oblate dust grains with axis ratios, i.e., the ratio between long and short axis of the grain, in the range of 1.1 to 4. For an overview of the parameters considered in our study, see Table A1. The absorption cross sections were obtained using a code developed by N. Voshchinnikov,[4] which is based on Voshchinnikov & Farafonov (1993). We note that the calculated degree of polarization using equation (A1) represents the polarization degree that would be observed in the ideal case in which every dust grain in the dust grain composition is perfectly aligned with respect to the magnetic field and there are no inclination or line-of-sights effects that may reduce the observed degree of polarization. Therefore, in a realistic case, the degree of polarization would be lower. To compensate this circumstance, we introduce a parameter (α) that is used as a scaling factor to artificially reduce the calculated degree of polarization. For one specific case, this parameter is applied uniformly to all wavelengths.

[4] http://www.astro.spbu.ru/DOP/6-SOFT/SPHEROID/1-SPH_new/.

Silicate dust phase

The results for the calculated degree of polarization for oblate dust grains which have an axis ratio of 2 and are consisting of pure astrosilicate, is shown in Figure A1. The error bars shown indicate the average polarization degree at 154, 214, and 850 μm (average polarization degree within 0.07 and 0.27 I/I_{max}, see Figure 2). In this case, every maximum dust grain size fits the observations (except $a_{max} = 10$ μm). The same holds true for every other axis ratio (1.1, 1.5, 3, 4; see Figure A4). The results are the same, we only have to adjust the α-parameter accordingly. In this case, we cannot constrain any properties of the dust in CB54.

Sil-Graph dust phase

The results for the calculated degree of polarization for nonspherical dust grains with an axis ratio of $a/b = 1.1$, consisting of Sil-Graph, is shown in Figure A2. The results shown here represent the ideal case, i.e., $\alpha = 1$. Even in this ideal case, the calculated degree of polarization is too low. Therefore, in this case, the axis ratio needs to be greater than 1.1 to match the observations.

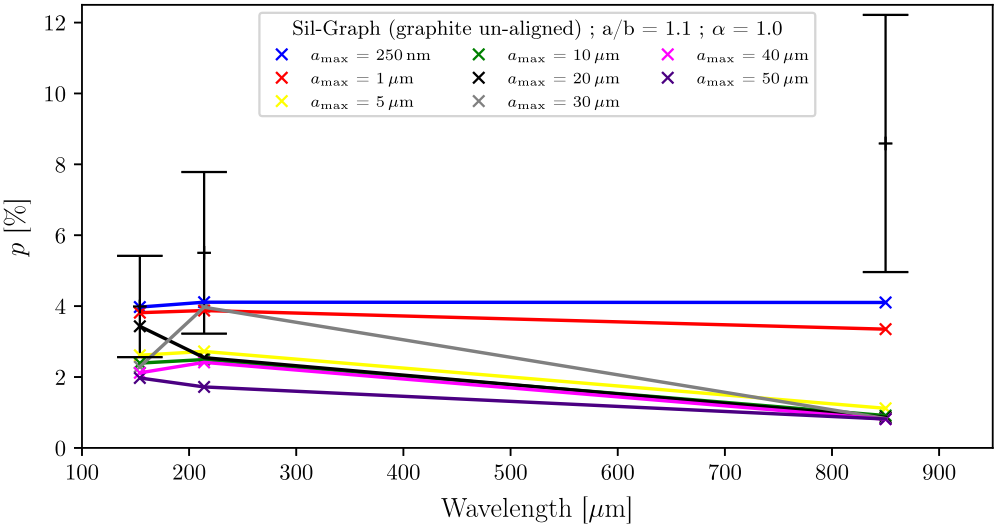

FIGURE A2 Calculated degree of polarization ("x" markers) using Equation (A1) for Sil-Graph grains with an axis ratio of 1.1. The error bars indicate the average polarization degree for the observations at 154, 214, and 850 μm.

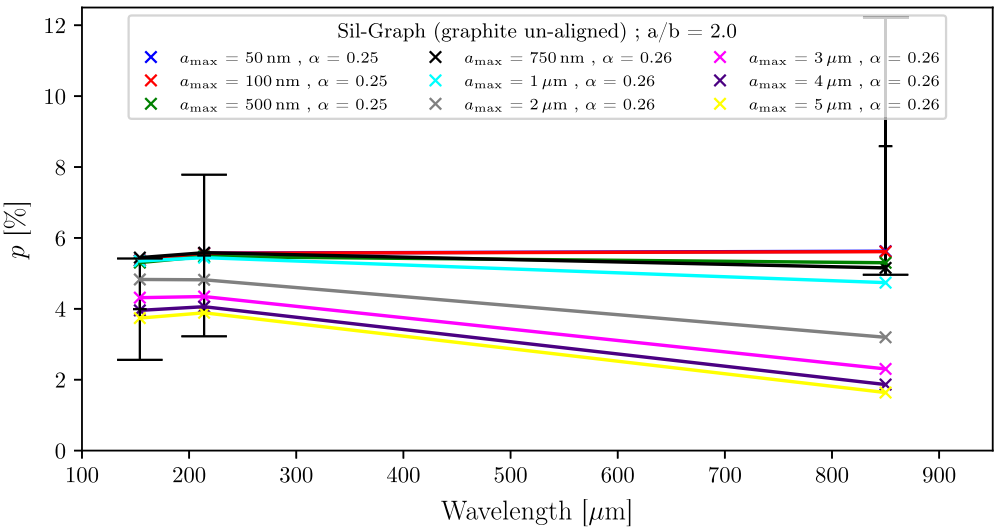

FIGURE A3 Calculated degree of polarization ("x" markers) using Equation (A1) for Sil-Graph grains with an axis ratio of 2. The error bars indicate the average polarization degree for the observations at 154, 214, and 850 μm.

The results for the calculated degree of polarization for oblate dust grains consisting of Sil-Graph with an axis ratio of $a/b = 2$, is shown in Figure A3. Here, we analyze dust with maximum grain sizes $a_{\rm max} \in (50\,{\rm nm} - 5\,\mu{\rm m})$. Maximum dust grain sizes of up to 0.75 μm allow us to fit the observations. If we assume an axis ratio of $a/b = 4$, $a_{\rm max} = 1\,\mu$m is found (see Figure A4).

In summary, the following constraints for the dust properties can be derived. Assuming pure astrosilicate dust grains, we cannot constrain any dust parameters. Assuming a mixture of silicate and graphite, the dust in CB54 needs to have an axis ratio $a/b > 1.1$. Additionally, the maximum dust grain size $a_{\rm max}$ is $\leq 0.75\,\mu$m ($\leq 1\,\mu$m for $a/b = 4$). This finding is similar to the result of Zielinski et al. (2021), who found $a_{\rm max} = 2\,\mu$m for the Bok globule B335 and Vaillancourt et al. (2020), who found $a_{\rm max} = 0.7\,\mu$m for the Taurus Cloud Complex.

We note that our results may drastically change if the graphite grains align with the magnetic field or other dust phases—like polycyclic aromatic hydrocarbons (PAH)—are considered. However, extending the parameter space in this direction is beyond the scope of our current study.

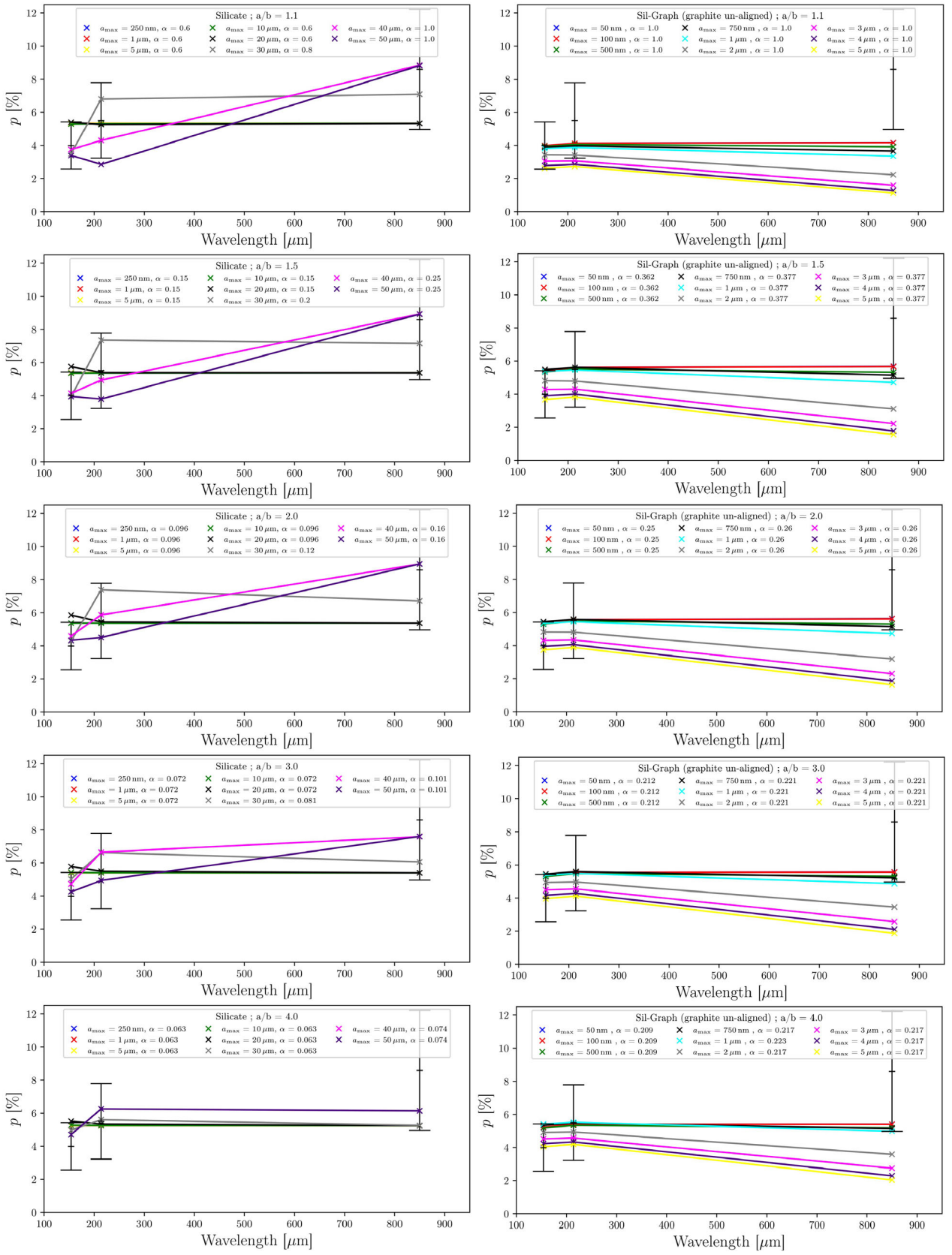

FIGURE A4 Overview of all calculated degree of polarization using Equation (A1) regarding the parameter study in the Appendix. *Left:* pure astrosilicate. *Right:* mixture of astrosilicate and graphite.